12

Spin Transition of Iron in Deep-Mantle Ferromagnesite

Jiachao Liu, Suyu Fu, and Jung-Fu Lin

ABSTRACT

Iron-bearing magnesite, or ferromagnesite ($[Mg,Fe]CO_3$), is an abundant component of Earth's deep-mantle carbonates. Under Earth's lower mantle pressure-temperature conditions, Fe^{2+} in $(Mg,Fe)CO_3$ undergoes an electronic high-spin (HS) to low-spin (LS) transition, which has been reported to influence a broad spectrum of the physical, chemical, and transport properties of the host ferromagnesite. These observations in turn help us better understand the effects of the Fe spin transition on other lower-mantle minerals. In this chapter, we review recent high-pressure experimental and theoretical results in the magnesite ($MgCO_3$) and siderite ($FeCO_3$) solid solution system. We first introduce the thermodynamic background of the Fe^{2+} spin transition in $(Mg,Fe)CO_3$ and summarize the characterizations of this transition using various high-pressure techniques. Using literature results, we focus on elucidating the effects of the Fe^{2+} spin transition on the equation of state, sound velocities, elastic moduli, and seismic radial anisotropies of $(Mg,Fe)CO_3$ in the Earth's mantle. Along an expected lower mantle geotherm, the Fe^{2+} spin crossover in $(Mg,Fe)CO_3$ occurs at ~ 50–80 GPa. Within this pressure range, the mixed-spin state of ferromagnesite exhibits significant increase in density but softening in V_P. Most significantly, $(Mg,Fe)CO_3$ exhibits a much higher V_S splitting anisotropy of ~45%–65% at lower mantle pressures compared with major candidate lower mantle minerals (e.g. ferropericlase: 3%–24%, bridgmanite: 11%–12% at 24–60 GPa). The strong anisotropy in textured $(Mg,Fe)CO_3$ developed due to its low strength could be used to explain high seismic *Vs* anisotropy observed in mantle subducting slabs at depths greater than 300 km. These observations suggest that $(Mg,Fe)CO_3$ as a deep-mantle carbon carrier can display unique physical and chemical properties.

12.1. INTRODUCTION

Carbonates are believed to be major deep-mantle carbon carriers that transport carbon stored in deep-sea sediments and oceanic mantle lithosphere (serpentinized and carbonated depleted peridotite) to the Earth's deep interior through subduction. The subduction of slabs with carbon-rich materials thus serves as a major influx source for the deep-Earth carbon cycle (e.g. Dasgupta & Hirschmann, 2010; Kelemen & Manning, 2015). At the same time, reduced carbon species such as diamond, Fe-C alloys, and carbon-bearing melts can return back to shallower depths along mantle upwellings and be oxidized to carbonates or carbonatite melts (Rohrbach & Schmidt, 2011). The presence of carbonates in subducting slabs may trigger deep-focus earthquakes and could be manifested in strong V_S radial anisotropy ($\xi = [V_{SH}/V_{SV}]^2$, where V_{SH} and V_{SV} are horizontally and vertically polarized shear waves, respectively) (J. Li et al., 2018). Therefore, studying the physical and chemical properties of carbonates under mantle pressure-temperature (P-T) conditions is critical for a better understanding of the deep carbon storage and cycling as well as its role in mantle geophysics and geochemistry.

Carbonates in the magnesite-siderite-calcite ($MgCO_3$-$FeCO_3$-$CaCO_3$) ternary system are the major forms of crustal and mantle carbonates. In most parts of the mantle, magnesite ($MgCO_3$) is the most abundant carbonate among these end members because of its

Department of Geological Sciences, Jackson School of Geosciences, University of Texas at Austin, Austin, Texas, USA

Carbon in Earth's Interior, Geophysical Monograph 249, First Edition. Edited by Craig E. Manning, Jung-Fu Lin, and Wendy L. Mao.

extensive P-T stability (Fiquet et al., 2002; Isshiki et al., 2004; Katsura & Ito, 1990; Z. Li et al., 2017; Tao et al., 2013). $MgCO_3$ and $FeCO_3$ form a complete solid solution series (Shatskiy et al., 2014), with the Mg-rich (Mg,Fe)CO_3 named as ferromagnesite and the Fe-rich (Mg,Fe)CO_3 named as magnesiosiderite. Previous experimental studies show that the coexisting ferromagnesite and olivine have comparable Fe/Mg ratios at 2.0-3.5 GPa and 1273–1373 K (Dalton & Wood, 1993), while Fe/Mg ratios in ferropericlase are 9–19 times higher than that of coexisting ferromagnesite at 6.5–7.5 GPa, 1273–1873 K (Palyanov et al., 2013). These partitioning data indicate that ferromagensite would be one of the most abundant and stable form of carbonates in the Earth's deep mantle. Siderite, on the other hand, may be unstable under most mantle P-T conditions (Cerantola et al., 2017; Tao et al., 2013). Subducted $CaCO_3$ and $CaMg(CO_3)_2$, on the other hand, could react with surrounding (Mg,Fe)SiO_3 and $(Mg,Fe)_2SiO_4$ to form $MgCO_3$ and $CaMg(SiO_3)_2$ (e.g. Biellmann et al., 1993; Kushiro, 1975; Jie Li et al., this monograph). Such chemical reactions would shift the compositions of deep mantle carbonates toward the (Mg,Fe)CO_3 compositional joint.

Fe is the most abundant 3d transition element in mantle minerals, and the variations in Fe electronic spin and valence states at mantle P-T conditions have been documented to play a significant role in controlling the geophysical and geochemical properties of the lower mantle ferropericlase (Fp) and bridgmanite (Bdg) (reviewed by Badro, 2014; Lin et al., 2013). This chapter focuses on the Fe^{2+} spin transition in (Mg,Fe)CO_3 and the corresponding effects on its physical and chemical properties, which include the density, sound velocity, elastic moduli, and V_S splitting anisotropy and their associated physical relevance to the spin transitions of Fp and Bdg in the lower mantle.

12.2. Fe^{2+} SPIN TRANSITION IN (MG,FE)CO_3

12.2.1. Crystal Field Theory and Parameters of the Spin Transition in Ferromagnesite

Ferromagnesite is stable with a rhombohedral structure in the $R\bar{3}c$ space group (Figure 12.1a). Mg^{2+} and Fe^{2+} occupy the octahedral sites composed of O^{2-} atoms, while the planar CO_3^{2-} units are perpendicular to the *c*-axis and the C-O bonds are parallel to the *a*-axis (Figure 12.1a). High-pressure single-crystal X-ray diffraction (XRD) measurements show that the octahedra are fairly isometric (Lavina, Dera, Downs, Yang, et al., 2010), which makes ferromagnesite an ideal case study for the spin transition behavior of Fe^{2+} in six-fold coordinated octahedral sites under high pressures. According to the symmetry of the charge density distribution and crystal field theory (Burns, 1993), the five 3*d*

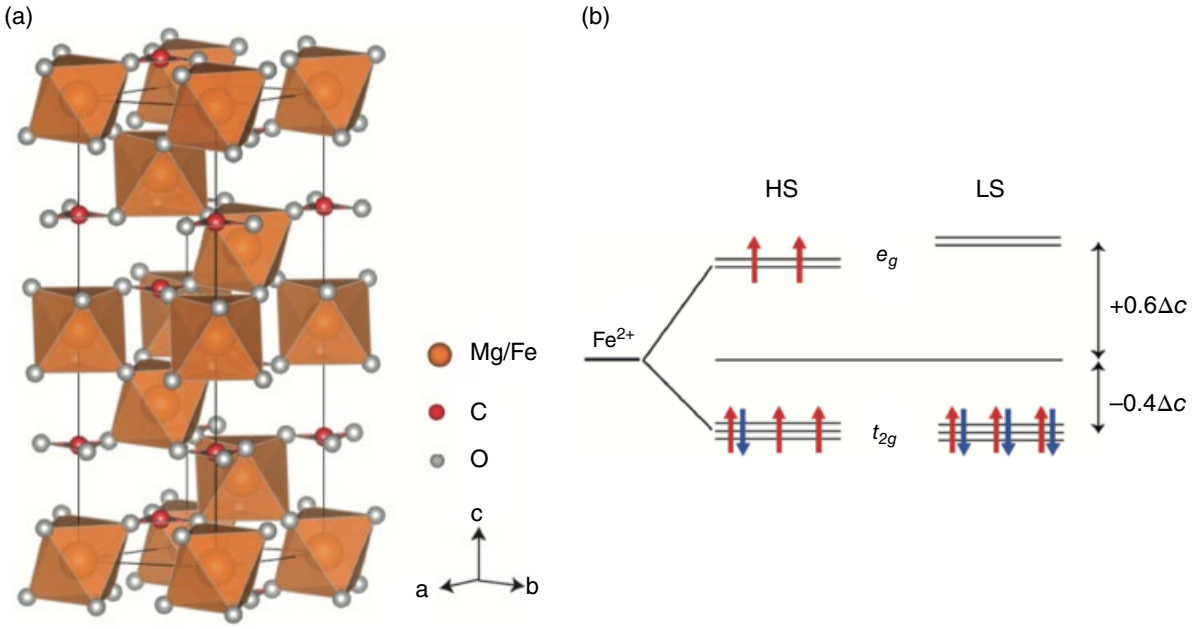

Figure 12.1 The crystal structure of rhombohedral (Mg,Fe)CO_3 and electronic structure of Fe^{2+} in (Mg,Fe)CO_3. (a) Rhombohedral (Mg,Fe)CO_3 is in $R\bar{3}c$ space group (Lavina et al., 2009). Mg^{2+} and Fe^{2+} occupy the octahedral sites shown as orange boxes. (b) Crystal field splitting diagrams of Fe^{2+} in the high-spin and low-spin states in the octahedral site. Δc is the crystal field splitting parameter; t_{2g} orbitals localize charge density between the coordinate axes; e_g orbitals localize charge density along the coordinate axes. See electronic version for color representation of the figures in this book.

orbitals of Fe^{2+} in the octahedral site of ferromagnesite are divided into two groups in a Cartesian coordination system: a set of three orbitals (d_{xy}, d_{xz}, d_{yz}) localize charge density between the coordinate axes, named as t_{2g} orbitals; the other two orbitals ($d_{x^2-y^2}$, d_{z^2}) with charge density concentrating along the coordinate axes are termed e_g orbitals. With the presence of oxygen ligands in the crystal structure, the degeneracy of the five *d*-orbitals of Fe^{2+} is lifted because of the different extent of the interaction between 3*d* electrons and ligands' electrons. As Fe^{2+} in $(Mg,Fe)CO_3$ occupies the six-fold coordinated octahedral site, e_g orbitals have higher energy than t_{2g} orbitals because of the proximity of e_g orbitals to the ligands (Burns, 1993). This results in an energy difference between e_g and t_{2g} orbitals, which is termed crystal-field splitting energy (Δc). The competition between Δc and the spin-paring energy Λ determines the electronic spin configuration of Fe^{2+} in $(Mg,Fe)CO_3$ (Figure 12.1). At ambient conditions where $\Delta c < \Lambda$, the number of paired electrons is minimized; therefore, Fe^{2+} in $(Mg,Fe)CO_3$ adopts a high-spin configuration with two paired electrons in one t_{2g} orbital, and the other four electrons are unpaired (Figure 12.1b). At higher pressures, the Fe-O bonds in $(Mg,Fe)CO_3$ are shortened (Lavina et al., 2009; Lavina, Dera, Downs, Tschauner, et al., 2010; Lavina, Dera, Downs, Yang, et al., 2010), resulting in a significant increase of Δc from ~14238 cm^{-1} (1.765 eV) to ~17517 cm^{-1} (2.172 eV) across the Fe^{2+} spin transition at 45.5 GPa and 300 K (Lobanov et al., 2015). In contrast, Λ is not sensitive to pressure increase as it is an intraionic quantity (Ohnishi, 1978), which is ~14193 cm^{-1} (1.760 eV) for siderite (Lobanov et al., 2015). Considering that the Fe-O length in $FeCO_3$ changes from 1.971 Å to 1.892 Å across the Fe^{2+} spin transition at ~45 GPa and 300 K (Lavina et al., 2010b), $\Delta c^{LS}/\Delta c^{HS}$ is comparable to $(r^{LS}/r^{HS})^{-5}_{Fe\text{-}O}$, consistent with theoretical prediction by Burns (1993). Once $\Delta c > \Lambda$ at ~ 45 GPa for $(Mg,Fe)CO_3$, all 3*d* electrons pair up in t_{2g} orbitals to form the LS state (Figure 12.1b). Optical absorption measurements have also been conducted for Fp and Bdg samples (e.g. Goncharov et al., 2006; Goncharov et al., 2008; Keppler et al., 2007, 2008), but the experimental results are still controversial due to Fe^{2+}-Fe^{3+} interaction and the complexity of crystal chemistry. Therefore, the change of Δc measured across the Fe^{2+} spin transition in $FeCO_3$ (Lobanov et al., 2015) provides the most solid experimental basis for understanding how the Fe^{2+} spin transition influences the thermal transport properties of lower-mantle minerals.

The change of Gibbs free energy $\Delta G_{LS\text{-}HS}$ across the Fe^{2+} spin transition can be expressed as follows (Sherman, 1988):

$$\Delta G_{LS-HS} = \Delta U_{LS-HS} + P\Delta V_{LS-HS} - T\Delta S_{LS-HS}, \quad (12.1)$$

where $\Delta U_{LS\text{-}HS}$, $\Delta V_{LS\text{-}HS}$, and $\Delta S_{LS\text{-}HS}$ are the differences in internal energy, volume, and entropy between LS and HS states, respectively; *P* is pressure; and *T* is temperature. Based on the crystal field theory (Burns, 1993), $\Delta U_{LS\text{-}HS}$ depends on the magnitudes of Δc and Λ. $\Delta V_{LS\text{-}HS}$ is negative because of the volume collapse across the spin transition (Lavina et al., 2009; Lavina, Dera, Downs, Tschauner, et al., 2010; Lavina, Dera, Downs, Yang, et al., 2010). Increasing pressure would promote the spin transition by lowering $\Delta G_{LS\text{-}HS}$ from a combined contribution of Δc and $\Delta V_{LS\text{-}HS}$. Increasing temperature, on the other hand, increases $\Delta G_{LS\text{-}HS}$ through the $-T\Delta S_{LS\text{-}HS}$ term in equation (12.1) and stabilizes the HS state with respect to the LS state. Two major components of $\Delta S_{LS\text{-}HS}$ are magnetic and configuration terms (Tsuchiya et al., 2006): The magnetic entropy for each spin state is expressed as $S_{mag} = k_B \ln[n\bullet(2S+1)]$ (Burns, 1993), where k_B is the Boltzmann constant, *S* is the total spin momentum of the 3*d* electrons in iron ion, and *n* is the electronic configuration degeneracy. Across the Fe^{2+} spin transition, S_{mag} decreases from $k_B \ln(15)$ to 0 ($S = 2$ and $n = 3$ for HS Fe^{2+}; $S = 0$, $n = 1$ for LS Fe^{2+} in $[Mg,Fe]CO_3$, respectively). Compared with spin transition pressure at 300 K, higher pressure is therefore needed to compensate the increases of $\Delta G_{LS\text{-}HS}$ from the $-T\Delta S_{LS\text{-}HS}$ term in equation (12.1) at high temperature condition. This is consistent with literature findings that pressures of the spin transition in $(Mg_{0.35}Fe_{0.65})CO_3$ increasing at a rate of ~10 MPa/K (Liu et al., 2014), indicating a generally positive Clapeyron slope. In addition, the configuration entropy of the coexisting HS and LS Fe^{2+} is defined as $S_{conf} = -k_B[n\ln n + (1-n)\ln(1-n)]$, where *n* is the LS fraction (Tsuchiya et al., 2006). High temperature condition would favor the mixed-spin state by decreasing ΔG_{mix} through the $-T\Delta S_{conf}$ term, which broadens the pressure range of the mixed-spin state. For example, the pressure interval of the mixed-spin state is ~4 GPa for $(Mg,Fe)CO_3$ at 300 K, but it broadens to ~10 GPa at 1200 K (Liu et al., 2014).

12.2.2. Characterizations of the Fe^{2+} Spin Transition in $(Mg,Fe)CO_3$ at High Pressure

The spin transition of Fe^{2+} in $(Mg,Fe)CO_3$ has been well constrained to occur at 40–50 GPa and 300 K using synchrotron X-ray and laser spectroscopies coupled with high-pressure diamond anvil cells (DAC) (Figure 12.2). The Fe^{2+} spin transition can cause significant changes in a range of physical properties of $(Mg,Fe)CO_3$, which in turn have been used to determine the occurrence of the Fe^{2+} spin transition. Specifically, the Fe^{2+} spin transition induces shortening of Fe-O bonds and lengthening of C-O bonds in $(Mg,Fe)CO_3$ (e.g. Lavina et al., 2010; Liu et al., 2019), which results in a reduction in the unit-cell volume and significant changes in vibrational properties

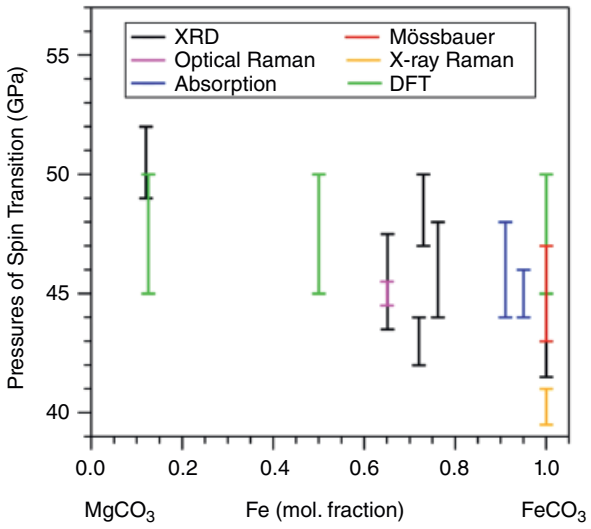

Figure 12.2 A summary of the reported pressure ranges for the Fe^{2+} spin transition in (Mg, Fe)CO_3 samples observed using various techniques at 300 K. Each vertical line with bars marks the pressure range of mixed-spin state for the corresponding composition. Black lines: XRD (Lavina et al., 2009; Lavina et al. 2010; Lavina et al., 2010; Nagai et al., 2010; Lin et al., 2012; Farfan et al., 2012; Liu et al., 2014, 2015); red line: Mössbauer (Cerantola et al., 2015, Liu et al., 2019); pink line: optical Raman (Lin et al. 2012); orange line: X-ray Raman (Weis et al., 2017); blue lines: optical absorption spectroscopy (Lobanov et al., 2015, 2016; Taran et al., 2017); green lines: DFT (Hsu & Huang, 2016). For simplicity, some previous DAC results obtained at relatively nonhydrostatic conditions, which can influence the spin transition pressure, are not shown here. See electronic version for color representation of the figures in this book.

(Cerantola et al., 2015; Lin et al., 2012; Spivak et al., 2014; Weis et al., 2017). Thus far, the Fe^{2+} spin transition in (Mg,Fe)CO_3 has been diagnosed based on the abrupt reduction of the unit-cell volume in XRD measurements (Farfan et al., 2012; Lavina et al., 2009; Lavina et al., 2010; Lavina et al., 2010; Lin et al., 2012; Liu et al., 2014, 2015; Nagai et al., 2010) and significant changes in the Raman shifts of vibrational modes in both optical and X-ray Raman spectroscopic studies (Cerantola et al., 2015; Fu et al., 2017; Lin et al., 2012; Spivak et al., 2014; Weis et al., 2017). Across the Fe^{2+} spin transition, the reduction of total spin momentum in Fe^{2+} can be captured by X-ray emission spectroscopy (Mattila et al., 2007). Conventional and synchrotron Mössbauer spectroscopies have also been used to study the Fe^{2+} spin transition in (Mg,Fe)CO_3 (Cerantola et al., 2015; Liu et al., 2019). Both of the fitted hyperfine parameters, center shift (CS) and quadrupole splitting (QS), show significant changes across the Fe spin transition, which have been used to determine spin transition pressures for not only (Mg,Fe)CO_3 (Cerantola et al., 2015) but also Fp and Bdg (e.g. Lin et al., 2013; Liu et al., 2018). In addition, the optical and near IR absorption spectra of (Mg,Fe)CO_3 also change significantly across the Fe^{2+} spin transition due to the dramatic increase in Δc (Lobanov et al., 2015, 2016; Taran et al., 2017). Theoretically, density function theory calculations predict the transition pressures that are in agreement with aforementioned experimental results (Hsu & Huang, 2016) (Figure 12.2). However, an early density function theory study underestimates the spin transition by ~15–30 GPa (Shi et al., 2008).

The starting pressure and pressure ranges of the Fe^{2+} spin transition in (Mg,Fe)CO_3 are sensitive to the hydrostatic condition in high-pressure DAC experiments: When relatively hydrostatic helium pressure medium is used in DAC experiments, the spin transition in $FeCO_3$ occurs at 40.4 ± 0.1 GPa with a transition width of 0.7 GPa at 300 K (Weis et al., 2017). In contrast, the spin transition pressure changes to 44.3 ± 0.4 GPa and the transition width broadens to 4.4 GPa when argon is used as the pressure medium (Weis et al., 2017). The Earth's mantle is mostly under relatively hydrostatic compression condition, except regions near subducting slabs where stress could be ~100–300 MPa (e.g. Houseman & Gubbins, 1997; Běhounková & Čížková, 2008). Therefore, hydrostatic results on the spin transition and its associated effects are certainly more applicable to the deep mantle. Specifically, it now becomes clearer that much of the inconsistencies in the study of the Fe spin transition in the lower mantle Fp is likely due to experimental conditions, together with possible iron clustering in the lattice (Kantor et al., 2009). Therefore, the broad spin transition pressures of $MgCO_3$-$FeCO_3$ observed in some DAC studies may be caused by artifacts from nonhydrostatic conditions. In addition, negligible compositional dependence of the spin transition pressures is found in (Mg,Fe)CO_3 (Figure 12.2). This is explained by weak Fe^{2+}-Fe^{2+} exchange interactions in (Mg,Fe)CO_3 due to the long distance between neighboring Fe^{2+} ions (3.458 Å at 1 bar, Lavina et al., 2010), which are separated by $(CO_3)^{2-}$ units along the *c*-axis (Figure 12.1a). In comparison, spin transition pressures of Fe^{2+} in Fp strongly depend on Fe content (Lin et al., 2006) because of the strong Fe^{2+}-Fe^{2+} exchange interactions, especially for FeO-rich magnesiowüstite.

12.2.3. The Effects of the Fe^{2+} Spin Transition on Physical Properties of (Mg,Fe)CO_3

12.2.3.1. Equation of State Anomaly Across the Fe^{2+} Spin Transition

The spin transition in (Mg,Fe)CO_3 is associated with a volume collapse due to the reconfiguration of the

electronic orbitals and thus shortening of the Fe-O bonds (e.g. Lavina et al., 2009; Lavina et al., 2010; Lavina et al., 2010; Lin et al., 2012; Liu et al., 2014). The relationship of pressure-volume-temperature, called the equation of state (EOS), is derived from high P-T XRD experiments in DACs and therefore can be used to infer the spin transition as well as the fraction of low spin Fe^{2+} (n_{LS}) at given P-T conditions. These XRD results have been used to model the EOS parameters across the spin transition and to construct the spin-crossover diagram at lower-mantle P-T conditions (e.g. Lavina et al., 2009; Lavina et al., 2010; Lavina et al., 2010; Lin et al., 2012; Liu et al., 2014).

A summary of the 300-K pressure-volume relationship for a range of compositions is shown in Figure 12.3a. The 1-bar unit cell volume of $(Mg,Fe)CO_3$ increases with Fe^{2+} content, consistent with the larger radius of HS Fe^{2+} (r ~ 0.92 Å; Shannon, 1976) than Mg^{2+} (r ~ 0.86 Å; Shannon, 1976) in the octahedral site (Figure 12.3b). In contrast, the fitted 1-bar unit cell volume of LS $(Mg,Fe)CO_3$ decreases with increasing Fe content (Figure 12.3b), which can be explained by the smaller radius of LS-Fe^{2+} (r ~ 0.75 Å; Shannon, 1976) in comparison with Mg^{2+}. These represent 8%–10% collapse of the 1-bar unit cell volume for Fe^{2+} ion from the HS to LS state in $(Mg,Fe)CO_3$ (Figure 12.3b). Further analysis of these results shows that the Fe^{2+} spin transition in $(Mg,Fe)CO_3$ induces a significant reduction in the unit-cell volume. For example, the unit-cell volumes of $(Mg_{0.35}Fe_{0.65})CO_3$ (Lin et al., 2012; Liu et al., 2014) and $FeCO_3$ (Lavina, Dera, Downs, Yang, et al., 2010) shrink by 6% and 10%, respectively, at around 45 GPa and 300 K (Figure 12.3a). The significant volume reduction caused by the Fe^{2+} spin transition makes the unit-cell volume of LS $(Mg,Fe)CO_3$ smaller than that of $MgCO_3$ (Figure 12.3a). The interatomic distances in $(Mg,Fe)CO_3$ are also significantly influenced by the Fe^{2+} spin transition: The shorter radius of LS Fe^{2+} decreases the Fe-O bond length by 0.078 Å at 45 GPa and 300 K for $FeCO_3$ (Lavina et al., 2010). The O-O bond lengths also shrink by 0.135–0.074 Å (Lavina et al., 2010). In contrast, the C-O bond exhibits lengthening across the Fe^{2+} spin transition, which may reflect a stress release of the C-O bond due to the shrinkage of the Fe-O bond (Lavina et al., 2010; Liu et al., 2019). The corresponding *a* and *c* axes shrink by 3% and 4%, respectively, for $FeCO_3$ (Lavina, Dera, Downs, Yang, et al., 2010) and 2% and 3%, respectively, for $(Mg_{0.35}Fe_{0.65})CO_3$ (Lin et al., 2012), which results in ~1% decrease in the *c*/*a* ratio (Lin et al., 2012). The higher compressibility of the *c*-axis compared with the *a*-axis can be explained by the rigidity of planar $(CO_3)^{2-}$ units (Lin et al., 2012), which are along the *a*-axis but perpendicular to the *c*-axis (Figure 12.1a). Based on the EOS modeling, the isothermal bulk moduli (K_T) of both HS and LS $(Mg,Fe)CO_3$ are not sensitive to its Fe content (Figure 12.3c), which can also be explained by the weak Fe^{2+}-Fe^{2+} exchange interactions (Lin et al., 2012). On the other

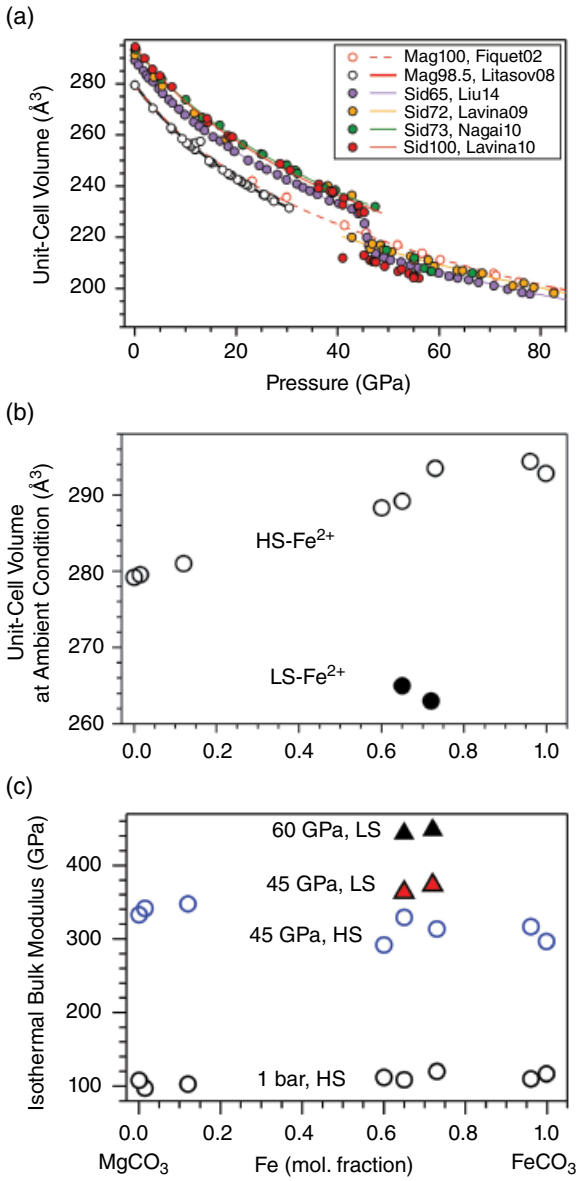

Figure 12.3 Spin transition of iron in $(Mg,Fe)CO_3$ at high pressure and 300 K. (a) A summary of compression curves for $(Mg,Fe)CO_3$ with different compositions at 300 K. (b) 1-bar and 300-K unit-cell volume (V_0) for high-spin Fe^{2+} (open circles) and fitted V_0 for low-spin Fe^{2+} (black circles) of $(Mg,Fe)CO_3$. (c) 300-K bulk moduli of $(Mg,Fe)CO_3$ at 1 bar (high-spin Fe^{2+}, open black circles), 45 GPa (high-spin Fe^{2+}, open blue circles), 45 GPa (low-spin Fe^{2+}, red triangles), and 60 GPa (low-spin Fe^{2+}, black triangles). Data sources are listed as follows: Fiquet02: (Fiquet et al., 2002); Litasov08: (Litasov et al., 2008); Liu14: (Liu et al., 2014); Lavina09: (Lavina et al., 2009); Nagai10: (Nagai et al., 2010); Lavina10: (Lavina et al., 2010). See electronic version for color representation of the figures in this book.

hand, the Fe^{2+} spin transition significantly influences the isothermal bulk modulus K_T (Figure 12.3c): K_T of LS (Mg,Fe)CO_3 is ~10%–19% larger than that of HS (Mg,Fe)CO_3 at 45 GPa and 300 K (Lavina et al., 2009; Lin et al., 2012; Liu et al., 2014). Within the pressure range of the mixed-spin state, the reduction of K_T is as high as ~86% for $(Mg_{0.35}Fe_{0.65})CO_3$ at 300 K (Liu et al., 2014), which is also associated with a significant decrease in elasticity and V_P (discussed in section 12.2.3.2). Such significant reduction in K_T results from the significant change in unit-cell volume ($\Delta V_{LS\text{-}HS}$), as dictated by the following equation from Wentzcovitch et al. (2009) based on an ideal mixing model:

$$\frac{V}{K} = \left(1 - n_{LS}\right)\frac{V_{HS}}{K_{HS}} + n_{LS}\frac{V_{LS}}{K_{LS}} - \left(V_{LS} - V_{HS}\right)\left(\frac{\partial n_{LS}}{\partial P}\right)_T \quad (12.2)$$

The thermal EOS results can be used to model the relevant thermoelastic parameters of (Mg,Fe)CO_3 along an expected mantle geotherm (Brown & Shankland, 1981). By using resistive and laser-heated DACs coupled with synchrotron XRD techniques, Liu et al. (2014) reported the P-T dependence of isothermal bulk modulus and thermal expansion coefficient. In addition, Liu et al. (2014, 2015) found that increasing temperature broadens the spin transition pressures of (Mg,Fe)CO_3 and the mixed-spin state would exist between ~53 and ~80 GPa along an expected geotherm (Brown & Shankland, 1981). Within the spin crossover, the magnitude of the unit-cell volume reduction relative to HS $(Mg_{0.35}Fe_{0.65})CO_3$ decreases from 6.0% at 300 K to 5.5% at 1200 K (Liu et al., 2014). Such P-T effects on the unit-cell volume translate into strong anomaly in the thermal expansion coefficient across the spin crossover (Liu et al., 2014). Compared with the HS counterpart, LS $(Mg_{0.35}Fe_{0.65})CO_3$ has ~10% higher bulk modulus and ~ 20% lower thermal expansion coefficient, making it 5%–7% denser than the HS phase at lower mantle P-T conditions. Therefore, dense LS ferromagnesite becomes thermodynamically more stable than its HS counterpart because of the negative $P\Delta V_{LS\text{-}HS}$ term in calculating $\Delta G_{LS\text{-}HS}$ (eq. [1]).

12.2.3.2. Anomalous Elastic Properties Across the Spin Transition

The concentration, valence, and spin states of Fe in mantle minerals could significantly influence the mantle seismic velocities, which could help explain some seismically observed heterogeneities (Fu et al., 2017; Liu et al., 2018; Wu & Wentzcovitch, 2014). The definitions of V_P and V_S splitting anisotropies are as follows:

$$A_P = 2\left(V_{P,\max} - V_{P,\min}\right)/\left(V_{P,\max} + V_{P,\min}\right) \times 100\% \quad (12.3)$$

$$A_S = 2\left(V_{S1} - V_{S2}\right)/\left(V_{S1} + V_{S2}\right) \times 100\%, \quad (12.4)$$

where $V_{P,max}$ and $V_{P,min}$ are the azimuthal maximum and minimum V_P, respectively, and V_{S1} and V_{S2} are two orthogonally polarized V_S velocities for a given propagation direction (Mainprice, 2015). Under the P-T conditions of the Earth's upper mantle, $MgCO_3$ exhibits 37%–41% V_P splitting anisotropy and 37%–41% V_S splitting anisotropy (Yang et al., 2014). The presence of Fe in (Mg,Fe)CO_3 together with its spin transition–induced elastic anomaly could further enhance the signatures of seismic velocity anisotropies.

The effect of the Fe^{2+} spin transition on the single-crystal elasticity of (Mg,Fe)CO_3 can be modeled using the following equation:

$$S^{ij}V\left(n\right) = nS^{ij}_{LS}V_{LS} + \left(1-n\right) S^{ij}_{HS}V_{HS} - \left(\frac{\partial G_{LS}}{\partial \sigma_j} - \frac{\partial G_{HS}}{\partial \sigma_j}\right)\frac{\partial n_{LS}}{\partial \sigma_i}, \quad (12.5)$$

where S^{ij} is the elastic compliance; σ_i and σ_j are the *ith* and *jth* stress components, respectively, in the Voigt notation; and G_{HS}, G_{LS} are the Gibbs free energies of the HS and LS states, respectively (Wu et al., 2013; Fu et al., 2017). The corresponding elastic constants C_{ij} can be calculated based on the relationship between C_{ij} and S^{ij} (Fu et al., 2017). The third term on the right-hand side of equation (12.5) determines the C_{ij} anomalies across the spin transition: $\frac{\partial n_{LS}}{\partial \sigma_i} \neq 0$ for $i = 1,2,3$ and $\frac{\partial n_{LS}}{\partial \sigma_i} = 0$ for $i = 4,5,6$. This is because n_{LS} is an even function of the shear stress components (Fu et al., 2017). As a result, drastic softening occurs on C_{11}, C_{12}, C_{13} and C_{33}, which are the elastic constants related to the compressional stress component. On the other hand, slight stiffening occurs on C_{14} and C_{44}, which are the elastic constants related to the shear stress component. Furthermore, calculating the aggregate elastic moduli (K_S and G) of ferromagnesite using Voigt-Reuss-Hill averages (Hill, 1952) shows that the calculation of K_S would involve all the softened elastic constants, C_{11}, C_{12}, C_{13}, and C_{33}, whereas the softening parts cancel out for the calculation of G (Fu et al., 2017). As a result, drastic softening in K_S and V_P and slight stiffening in G and V_S would be expected across the Fe^{2+} spin transition in (Mg,Fe)CO_3. Notably, equation (12.5) is also applicable to Fp and Bdg (Fu et al., 2018; Yang et al., 2015), both of which show significant softening in K_S and V_P but almost smooth profiles for G and V_S across the spin transition pressures of Fe^{2+} and Fe^{3+} in the octahedral sites of Fp and Bdg, respectively.

A recent experimental study using Brillouin light scattering (BLS) and impulsive stimulated light scattering (ISS) techniques has determined the effects of the Fe^{2+}

spin transition on the single-crystal elastic constants (C_{ij}) of $(Mg_{0.35}Fe_{0.65})CO_3$ (Fu et al., 2017). Within the pressure range of the Fe^{2+} spin transition, V_P and V_S of $(Mg_{0.35}Fe_{0.65})CO_3$ are reduced by as much as ~40% and ~21%, respectively, at 300 K (Figure 12.4), which are consistent with the thermodynamic predictions discussed above. However, the elastic moduli of $FeCO_3$ derived from the phonon dispersion frequency probed by the inelastic X-ray scattering technique do not show softening across the pressure range of the Fe^{2+} spin transition (Stekiel et al., 2017). Such an inconsistence has also been seen in sound velocity measurements of Fp samples (Antonangeli et al., 2011; Crowhurst et al., 2008; Yang et al., 2015), which could be explained by the different frequencies and scattering vectors used in inelastic X-ray scattering compared with BLS and ISS (Lin et al., 2013). Because BLS and ISS directly measure the acoustic wave velocities of samples, the effects of Fe^{2+} spin transition on the sound velocity of $(Mg,Fe)CO_3$ determined by these techniques are more applicable to seismic implications.

To quantitatively understand the effects of Fe on the elasticity of $(Mg,Fe)CO_3$, the velocities of $(Mg,Fe)CO_3$ at high pressures are compared with those of end-member $MgCO_3$ (Figure 12.4). At 1 bar to ~ 40 GPa, V_P and V_S of HS $(Mg_{0.35}Fe_{0.65})CO_3$ are ~17% and 22% lower than that of $MgCO_3$, respectively (Figure 12.4 b, c). Within the pressure range of the Fe^{2+} spin transition, V_P of $(Mg_{0.35}Fe_{0.65})CO_3$ is reduced by as much as 56% with respect to $MgCO_3$ (Figure 12.4 b, c). At higher pressures, there is ~9% reduction in both V_P and V_S for LS $(Mg_{0.35}Fe_{0.65})CO_3$, up to 70 GPa with respect to $MgCO_3$ (Figure 12.4 b, c). Assuming a linear relationship between velocities and Fe content, V_P would decrease with an average dV_P/dFe of about –0.026 km/s/mol.% for the HS state at 0–40 GPa and dV_P/dFe of about –0.0016 km/s/mol.% for the LS state at 40–60 GPa. V_S decreases with dV_S/dFe of about –0.019 km/s/mol.% for the HS state and dV_S/dFe of about –0.007 km/s/mol.% for the LS state. Compared with $MgCO_3$, the shear-wave splitting anisotropy factor A_S of $(Mg,Fe)CO_3$ increases, particularly across the pressure range of the Fe^{2+} spin transition (Figure 12.5). For $MgCO_3$, A_S increases from ~37% to ~48% with pressure increasing from 0 to 60 GPa (Yang et a., 2014; Stekiel et al., 2017). In comparison, A_S of $(Mg_{0.35}Fe_{0.65})CO_3$ increases from ~37% to ~58% between 1 bar and 40 GPa and reaches a peak at ~64% across the spin transition, but it decreases to ~53% for LS state at 47 GPa and 300 K (Figure 12.5). The V_S anisotropy factor of ferromagnesite across the spin transition is much higher than that of major lower-mantle minerals, such as Bdg with ~10%–20% A_S (Karki et al., 1997) and Fp with ~20% A_S under lower-mantle pressures (Marquardt et al., 2009; Yang et al., 2015). Here we interpolated the seismic properties of $(Mg_{0.90}Fe_{0.10})CO_3$ from those of $MgCO_3$ and magnesiosiderite compositions (Figures 12.4 and 12.5). The

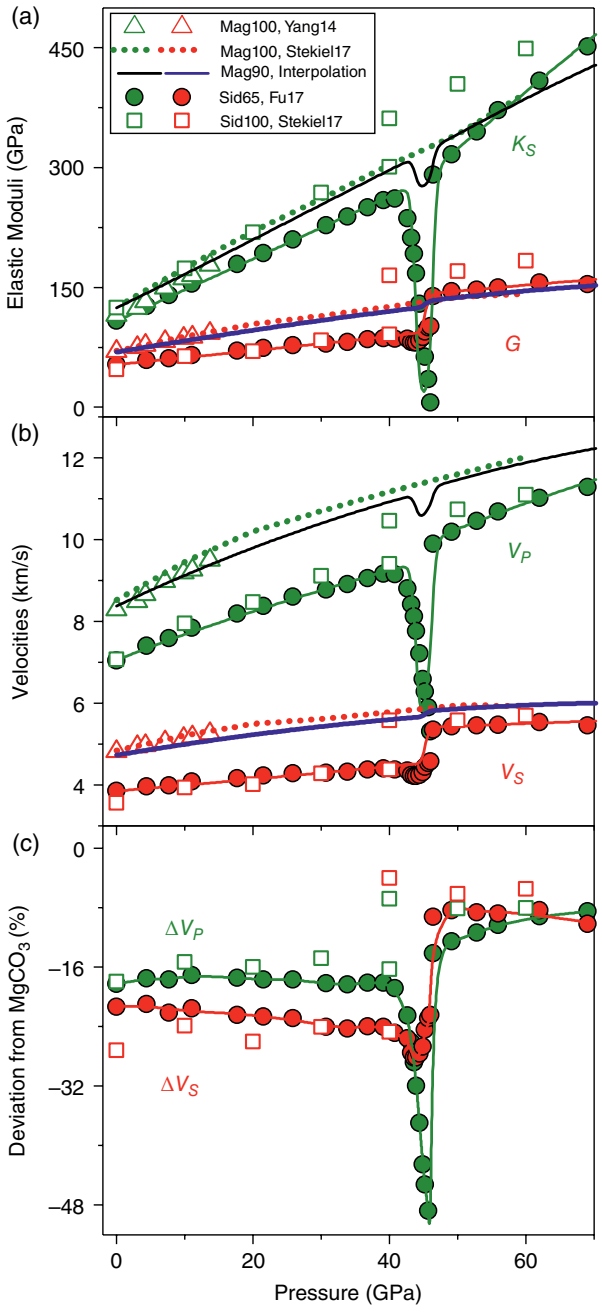

Figure 12.4 The pressure dependence of the elastic properties of $(Mg,Fe)CO_3$ at high pressure and 300 K. (a) and (b) Aggregate elastic properties (K_S, G, V_P, V_S) of $(Mg,Fe)CO_3$ with different iron contents; (c) Deviations of sound velocities in Fe-bearing $(Mg,Fe)CO_3$ with respect to $MgCO_3$ magnesite. Data source: open squares, $FeCO_3$ from inelastic X-ray scattering measurements (Stekiel et al., 2017); open triangles, $MgCO_3$ from BLS measurements (Yang et al., 2014); solid circles, $(Mg_{0.35}Fe_{0.65})CO_3$ using BLS and ISS measurements (Fu et al., 2017); solid curves, fittings to results of Fu et al. (2017); dotted curves, $MgCO_3$ using DFT calculation (Stekiel et al., 2017); black and blue curves, interpolated results for $(Mg_{0.90}Fe_{0.10})CO_3$. See electronic version for color representation of the figures in this book.

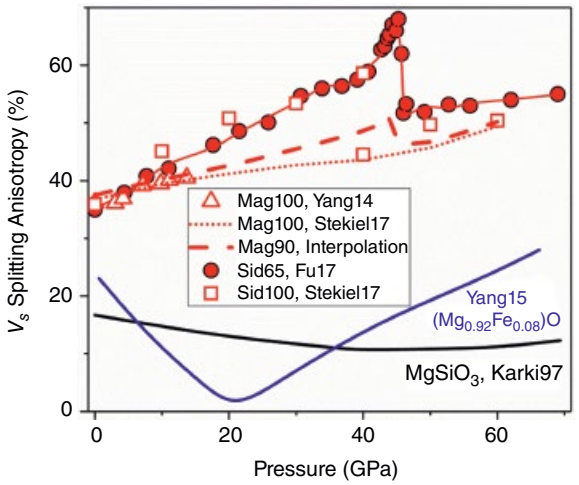

Figure 12.5 The pressure dependence of the V_S anisotropy factor (A_S) of $(Mg,Fe)CO_3$ in comparison with those of $MgSiO_3$ bridgmanite and $(Mg_{0.92}Fe_{0.08})O$ ferropericlase at high pressure and 300 K. The data sources for $(Mg,Fe)CO_3$ are the same as for Figure 12.4. The anisotropy factor of $MgSiO_3$ bridgmanite and $(Mg_{0.92}Fe_{0.08})O$ Fp are from Karki et al. (1997) and Yang et al. (2015), respectively. See electronic version for color representation of the figures in this book.

modeled results show ~5% decrease in V_P and ~2% increase in V_S would occur in $(Mg_{0.90}Fe_{0.10})CO_3$ across the spin transition region. A_S of $(Mg_{0.90}Fe_{0.10})CO_3$ is comparable with that of $MgCO_3$ in the upper mantle, but 5% and 13% higher at the bottom of the transition zone and the middle mantle, respectively (Figure 12.5). At deeper depths, A_S of LS $(Mg_{0.90}Fe_{0.10})CO_3$ becomes comparable with that of $MgCO_3$ again (Figure 12.5). In addition, A_S of HS $(Mg_{0.90}Fe_{0.10})CO_3$ is about 4–13 times higher than those of the two major lower-mantle minerals, Bdg and Fp, at the uppermost lower mantle depths; in the middle mantle depths, A_S of LS $(Mg_{0.90}Fe_{0.10})CO_3$ is about 2–4 times higher than those of Bdg and Fp (Figure 12.5).

In the mantle, especially near the subduction regions, deformation-induced lattice-preferred orientations of minerals together with their A_S could generate seismic V_S radial anisotropy (e.g. Panning & Romanowicz, 2004; Wookey and Kendall, 2004). Previous deformation experiments show that the strength of $MgCO_3$ is several orders of magnitude lower than peridotite at mantle P-T conditions (Holyoke et al., 2014). By analyzing the micro-structures and lattice orientations of recovered $MgCO_3$ samples from deformation experiments, Ulrich (2015) found that the *c*-axis tends to parallel to the maximum compressive stress under high P-T conditions. These experimental results indicate that ferromagnesite conveyed by subducting slabs would localize strain and develop a lattice-preferred orientation with the *c*-axis parallel to the maximum compressive stress. Together with its strong anisotropy, ferromagenesite would be a leading candidate for explaining the strong seismic anisotropy. A recent seismic study observed strong seismic anisotropy of ~25% below ~300 km (J. Li et al., 2018), which is attributed to the presence of either magnesite or carbonatite melt. The addition of Fe^{2+} into magnesite and the associated increase of A_S due to Fe^{2+} spin transition from the bottom of the transition zone to the middle lower mantle (Figure 12.5) would further promote ferromagnesite as a leading candidate to explain seismic anisotropy near the subduction regions (J. Li et al., 2018).

12.3. CONCLUSIONS

The pressure-temperature conditions of the Fe^{2+} spin transition in ferromagnesite $(Mg,Fe)CO_3$ and its influence on the geophysical properties of this mantle major carbonate have been extensively studied by both experimental and theoretical methods. Along an expected mantle geotherm, the Fe^{2+} spin transition in ferromagnesite is expected to occur at ~50–80 GPa. Within this pressure range, significant density increase, V_P softening and slight V_S stiffening are expected. At deeper depths, ferromagnesite with low-spin Fe^{2+} would have higher density, incompressibility, and sound velocities than its high-spin Fe^{2+} counterpart. The strong anisotropy and low strength of ferromagnesite make it a potential candidate to explain the strong seismic radial anisotropy in the subduction regions beneath 300 km. Moreover, the robust results on the Fe^{2+} spin transition and its associated changes in the physical properties of ferromagnesite would provide the baseline for understanding the iron spin transition in the lower-mantle ferropericlase and bridgmanite.

Future work could focus on determining how spin states of Fe^{2+} influence iron partitioning, especially across melting temperature, as well as the rheological and transport properties of $(Mg,Fe)CO_3$ at lower-mantle P-T conditions. For example, based on the change of the crystal-field splitting energy across the spin transition in $(Mg,Fe)CO_3$, Lobanov et al. (2015) infer that Fe would strongly partition into low-spin $(Mg,Fe)CO_3$ compared with coexisting bridgmanite. Upon melting, Fe^{2+} in carbonated melt can also experience a spin transition, which may also significantly influence Fe partitioning (Fu et al., 2018). In addition, the relationship between the spin states of Fe^{2+} and the crystal structures/chemical compositions of carbonates under the lower-mantle conditions would shed light on the fate of these oxidized components in the reduced lower mantle.

ACKNOWLEDGMENTS

The authors acknowledge the support of the Deep Carbon Observatory and Geophysics Program of the National Science Foundation.

REFERENCES

Antonangeli, D., Siebert, J., Aracne, C. M., Farber, D. L., Bosak, A., Hoesch, M., et al. (2011). Spin crossover in ferropericlase at high pressure: A seismologically transparent transition? *Science*, *331*, 64–67.

Badro, J. (2014). Spin transitions in mantle minerals. *Annu Rev Earth Pl Sc*, *42*, 231–248.

Běhounková, M., & Čížková, H. (2008). Long-wavelength character of subducted slabs in the lower mantle. *Earth and Planetary Science Letters*, *275*, 43–53.

Biellmann, C., Gillet, P., Guyot, F., Peyronneau, J., & Reynard, B. (1993). Experimental evidence for carbonate stability in the Earth's lower mantle. *Earth and Planetary Science Letters*, *118*, 31–41.

Brown, J. M., & Shankland, T. J. (1981). Thermodynamic parameters in the Earth as determined from seismic profiles. *Geophysical Journal of the Royal Astronomical Society 66*, 579–596.

Burns, R. G. (1993). *Mineralogical applications of crystal field theory*. Cambridge, UK: Cambridge University Press.

Cerantola, V., Bykova, E., Kupenko, I., Merlini, M., Ismailova, L., McCammon, C., et al. (2017). Stability of iron-bearing carbonates in the deep Earth's interior. *Nature Communications*, *8*, 15960.

Cerantola, V., McCammon, C., Kupenko, I., Kantor, I., Marini, C., Wilke, M., et al. (2015). High-pressure spectroscopic study of siderite ($FeCO_3$) with a focus on spin crossover. *American Mineralogist*, *100*, 2670–2681.

Crowhurst, J. C., Brown, J. M., Goncharov, A. F., & Jacobsen, S. D. (2008). Elasticity of (Mg,Fe)O through the spin transition of iron in the lower mantle. *Science*, *319*, 451–453.

Dalton, J. A., & Wood, B. J. (1993). The partitioning of Fe and Mg between olivine and carbonate and the stability of carbonate under mantle conditions. *Contrib Mineral Petr*, *114*, 501–509.

Dasgupta, R., & Hirschmann, M. M. (2010). The deep carbon cycle and melting in Earth's interior. *Earth Planet Sci Lett*, *298*, 1–13.

Farfan, G., Wang, S., Ma, H., Caracas, R., & Mao, W.L. (2012). Bonding and structural changes in siderite at high pressure. *American Mineralogist*, *97*, 1421–1426.

Fiquet, G., Guyot, F., Kunz, M., Matas, J., Andrault, D., & Hanfland, M. (2002). Structural refinements of magnesite at very high pressure. *American Mineralogist*, *87*, 1261–1265.

Fu, S., Yang, J., & Lin, J.-F. (2017). Abnormal elasticity of single-crystal magnesiosiderite across the spin transition in Earth's lower mantle. *Phys. Rev. Lett.*, *118*, 036402.

Fu, S., Yang, J., Zhang, Y., Liu, J., Greenberg, E., Prakapenka, V.B., et al. (2018). Melting behavior of the lower-mantle ferropericlase across the spin crossover: Implication for the ultra-low velocity zones at the lowermost mantle. *Earth and Planetary Science Letters*, *503*, 1–9.

Fu, S., Yang, J., Zhang, Y., Okuchi, T., McCammon, C., Kim, H.-I., et al. (2018). Abnormal elasticity of Fe-bearing bridgmanite in the Earth's lower mantle. *Geophysical Research Letters*, *45*, 4725–4732.

Goncharov, A. F., Haugen, B. D., Struzhkin, V. V., Beck, P., & Jacobsen, S. D. (2008). Radiative conductivity in the Earth's lower mantle. *Nature*, *456*, 231–234.

Goncharov, A. F., Struzhkin, V. V., & Jacobsen, S. D. (2006). Reduced radiative conductivity of low-spin (Mg,Fe)O in the lower mantle. *Science*, *312*, 1205–1208.

Hill, R. (1952). The elastic behaviour of a crystalline aggregate. *Proceedings of the Physical Society. Section A*, *65*, 349.

Holyoke, C. W., Kronenberg, A. K., Newman, J., & Ulrich, C. (2014). Rheology of magnesite. *Journal of Geophysical Research: Solid Earth*, *119*, 6534–6557.

Houseman, G. A., & Gubbins, D. (1997). Deformation of subducted oceanic lithosphere. *Geophys J Int*, *131*, 535–551.

Hsu, H., & Huang, S.-C. (2016). Spin crossover and hyperfine interactions of iron in $(Mg,Fe)CO_3$ ferromagnesite. *Phys. Rev. B*, *94*, 060404.

Isshiki, M., Irifune, T., Hirose, K., Ono, S., Ohishi, Y., Watanuki, T., et al. (2004). Stability of magnesite and its high-pressure form in the lowermost mantle. *Natur,e 427*, 60–63.

Kantor, I., Dubrovinsky, L., McCammon, C., Steinle-Neumann, G., Kantor, A., Skorodumova, N., et al. (2009). Short-range order and Fe clustering in $Mg_{1-x}Fe_xO$ under high pressure. *Phys. Rev. B*, *80*, 014204.

Karki, B. et al. (1997). Elastic properties of orthorhombic MgSiO3 perovskite at lower mantle pressures. *Am Mineral*, *82*, 635–638.

Katsura, T., & Ito, E. (1990). Melting and subsolidus phase relations in the $MgSiO_3$-$MgCO_3$ system at high pressures: implications to evolution of the Earth's atmosphere. *Earth and Planetary Science Letters*, *99*, 110–117.

Kelemen, P. B., & Manning, C. E. (2015). Reevaluating carbon fluxes in subduction zones, what goes down, mostly comes up. *P Natl Acad Sci USA 112*, E3997–E4006.

Keppler, H., Dubrovinsky, L. S., Narygina, O., & Kantor, I. (2008). Optical absorption and radiative thermal conductivity of silicate perovskite to 125 gigapascals. *Science*, *322*, 1529–1532.

Keppler, H., Kantor, I., & Dubrovinsky, L. S. (2007). Optical absorption spectra of ferropericlase to 84 GPa. *Am Mineral*, *92*, 433–436.

Kushiro, I. (1975). Carbonate-silicate reactions at high pressures and possible presence of dolomite and magnesite in the upper mantle. *Earth and Planetary Science Letters*, *28*, 116–120.

Lavina, B., Dera, P., Downs, R. T., Prakapenka, V., Rivers, M., Sutton, S., & Nicol, M. (2009). Siderite at lower mantle conditions and the effects of the pressure-induced spin-pairing transition. *Geophys. Res. Lett.*, *36*, L23306.

Lavina, B., Dera, P., Downs, R. T., Tschauner, O., Yang, W., Shebanova, O., & Shen, G. (2010). Effect of dilution on the spin pairing transition in rhombohedral carbonates. *High Pressure Research*, *30*, 224–229.

Lavina, B., Dera, P., Downs, R. T., Yang, W., Sinogeikin, S., Meng, Y., et al. (2010). Structure of siderite $FeCO_3$ to 56 GPa and hysteresis of its spin-pairing transition. *Phys. Rev. B*, *82*, 064110.

Li, J., Zheng, Y., Thomsen, L., Lapen, T. J., & Fang, X. (2018). Deep earthquakes in subducting slabs hosted in highly anisotropic rock fabric. *Nature Geoscience*, *11*, 696.

Li, Z., Li, J., Lange, R., Liu, J., & Militzer, B. (2017). Determination of calcium carbonate and sodium carbonate melting curves up to Earth's transition zone pressures with

implications for the deep carbon cycle. *Earth and Planetary Science Letters*, *457*, 395–402.

Lin, J.-F., Gavriliuk, A. G., Struzhkin, V. V., Jacobsen, S. D., Sturhahn, W., Hu, M. Y., et al. (2006). Pressure-induced electronic spin transition of iron in magnesiowustite-(Mg,Fe) O. *Phys. Rev. B*, *73*, 113107.

Lin, J.-F., Liu, J., Jacobs, C., & Prakapenka, V. B. (2012). Vibrational and elastic properties of ferromagnesite across the electronic spin-pairing transition of iron. *American Mineralogist*, *97*, 583–591.

Lin, J.-F., Speziale, S., Mao, Z., & Marquardt, H. (2013). Effects of the electronic spin transitions of iron in lower mantle minerals: implications for deep mantle geophysics and geochemistry. *rev. geophys. 51*, 244–275.

Litasov, K. D., Fei, Y., Ohtani, E., Kuribayashi, T., & Funakoshi, K. (2008). Thermal equation of state of magnesite to 32 GPa and 2073 K. *Physics of the Earth and Planetery Interiors*, *168*, 191–203.

Liu, J., Dorfman, S.M., Zhu, F., Li, J., Wang, Y., Zhang, D., et al. (2018). Valence and spin states of iron are invisible in Earth's lower mantle. *Nature Communications*, *9*, Article 1284.

Liu, J., Lin, J.-F., Mao, Z., & Prakapenka, V. B. (2014). Thermal equation of state and spin transition of magnesiosiderite at high pressure and temperature. *American Mineralogist*, *99*, 84–93.

Liu, J., Lin, J.-F., & Prakapenka, V. B. (2015). High-pressure orthorhombic ferromagnesite as a potential deep-mantle carbon carrier. *Scientific Reports 5*, srep07640.

Liu, J., Wang, W., Yang, H., Wu, Z., Hu, M., Zhao, J., et al. (2019). Carbon isotopic signatures of super-deep diamonds mediated by iron redox chemistry. *Geochemical Perspectives Letters*. doi: 10.7185/geochemlet.1915

Lobanov, S. S., Goncharov, A. F., & Litasov, K. D. (2015). Optical properties of siderite ($FeCO_3$) across the spin transition: Crossover to iron-rich carbonates in the lower mantle. *American Mineralogist*, *100*, 1059–1064.

Lobanov, S. S., Holtgrewe, N., & Goncharov, A. F. (2016). Reduced radiative conductivity of low spin FeO_6-octahedra in $FeCO_3$ at high pressure and temperature. *Earth and Planetary Science Letters*, *449*, 20–25.

Mainprice, D. (2015). Seismic anisotropy of the deep Earth from a mineral and rock physics perspective. In G. Schubert (Ed.), *Treatise on geophysics* (2nd ed., pp. 487–538). Oxford: Elsevier.

Marquardt, H., Speziale, S., Reichmann, H. J., Frost, D. J., & Schilling, F. R. (2009). Single-crystal elasticity of $(Mg_{0.9}Fe_{0.1})$ O to 81 GPa. *Earth and Planetary Science Letters*, *287*, 345–352.

Mattila, A., Pylkkänen, T., Rueff, J.-P., Huotari, S., Vankó, G., Hanfland, M., et al. (2007). Pressure induced magnetic transition in siderite $FeCO_3$ studied by x-ray emission spectroscopy. *J. Phys.: Condens. Matter*, *19*, 386206.

Nagai, T., Ishido, T., Seto, Y., Nishio-Hamane, D., Sata, N., & Fujino, K. (2010). Pressure-induced spin transition in $FeCO_3$-siderite studied by X-ray diffraction measurements. *J. Phys.: Conf. Ser.*, *215*, 012002.

Ohnishi, S. (1978). A theory of the pressure-induced high-spin-low-spin transition of transition-metal oxides. *Physics of the Earth and Planetary Interiors*, *17*, 130–139.

Palyanov, Y. N., Bataleva, Y. V., Sokol, A. G., Borzdov, Y. M., Kupriyanov, I. N., Reutsky, V. N., & Sobolev, N. V. (2013). Mantle-slab interaction and redox maechanism of diamond formation. *PNAS*, *110*, 20408–20413.

Panning, M., & Romanowicz, B. (2004). Inferences on flow at the base of Earth's mantle based on seismic anisotropy. *Science*, *303*, 351–353.

Rohrbach, A., & Schmidt, M. W. (2011). Redox freezing and melting in the Earth's deep mantle resulting from carbon-iron redox coupling. *Nature*, *472*, 209–212.

Shannon, R. D. (1976). Revised effective ionic radii and systematic studies of interatomic distances in halides and chalcogenides. *Acta Crystallographica Section A: Crystal Physics, Diffraction, Theoretical and General Crystallography*, *32*, 751–767.

Shatskiy, A., Borzdov, Y. M., Litasov, K. D., Kupriyanov, I. N., Ohtani, E., & Palyanov, Y. N. (2014). Phase relations in the system $FeCO_3$-$CaCO_3$ at 6 GPa and 900–1700 °C and its relation to the system $CaCO_3$-$FeCO_3$-$MgCO_3$. *American Mineralogist*, *99*, 773–785.

Sherman, D. M. (1988). High-spin to low-spin transition of iron(II) oxides at high pressures: Possible effects on the physics and chemistry of the lower mantle. In S. Ghose, J.M.D. Coey, & E. Salje (Eds.), *Structural and magnetic phase transitions in minerals: Advances in physical geochemistry* (pp. 113–128). New York: Springer.

Shi, H., Luo, W., Johansson, B., & Ahuja, R. (2008). First-principles calculations of the electronic structure and pressure-induced magnetic transition in siderite $FeCO_3$. *Phys. Rev. B*, *78*, 155119.

Spivak, A., Solopova, N., Cerantola, V., Bykova, E., Zakharchenko, E., Dubrovinsky, L., & Litvin, Y. (2014). Raman study of $MgCO_3$–$FeCO_3$ carbonate solid solution at high pressures up to 55 GPa. *Phys Chem Minerals*, *41*, 633–638.

Stekiel, M., Nguyen-Thanh, T., Chariton, S., McCammon, C., Bosak, A., & Morgenroth, W. (2017). High pressure elasticity of $FeCO_3$-$MgCO_3$ carbonates. *Physics of the Earth and Planetary Interiors*, *271*, 57–63.

Tao, R., Fei, Y., & Zhang, L. (2013). Experimental determination of siderite stability at high pressure. *American Mineralogist*, *98*, 1565–1572.

Taran, M. N., Müller, J., Friedrich, A., & Koch-Müller, M. (2017). High-pressure optical spectroscopy study of natural siderite. *Phys Chem Minerals*, *44*, 537–546.

Tsuchiya, T., Wentzcovitch, R. M., da Silva, C.R.S., & de Gironcoli, S. (2006). Spin transition in magnesiowüstite in Earth's lower mantle. *Phys. Rev. Lett. 96*, 198501.

Ulrich, C. A, (2015). *Deformation mechanisms and microstructures of experimentally deformed magnesite*. Master's thesis, Texas A & M University.

Weis, C., Sternemann, C., Cerantola, V., Sahle, C. J., Spiekermann, G., Harder, M., et al. (2017). Pressure driven spin transition in siderite and magnesiosiderite single crystals. *Scientific Reports*, *7*, 16526.

Wentzcovitch, R. M., Justo, J. F., Wu, Z., da Silva, C.R.S., Yuen, D. A., & Kohlstedt, D. (2009). Anomalous compressibility of ferropericlase throughout the iron spin cross-over. *P Natl Acad Sci USA*, *106*, 8447–8452.

Wookey, J., & Kendall, J.-M. (2004). Evidence of midmantle anisotropy from shear wave splitting and the influence of shear-coupled P waves. *Journal of Geophysical Research: Solid Earth*, *109*.

Wu, Z., Justo, J. F., & Wentzcovitch, R M. (2013). Elastic anomalies in a spin-crossover system: ferropericlase at lower mantle conditions. *Phys. Rev. Lett.*, *110*, 228501.

Wu, Z., & Wentzcovitch, R. M. (2014). Spin crossover in ferropericlase and velocity heterogeneities in the lower mantle. *P Natl Acad Sci USA*, *111*, 10468–10472.

Yang, J., Mao, Z., Lin, J.-F., & Prakapenka, V. B. (2014). Single-crystal elasticity of the deep-mantle magnesite at high pressure and temperature. *Earth and Planetary Science Letters*, *392*, 292–299.

Yang, J., Tong, X. Y., Lin, J. F., Okuchi, T., & Tomioka, N. (2015). Elasticity of ferropericlase across the spin crossover in the Earth's lower mantle. *Sci Rep-Uk 5*.